ORIGINAL ARTICLE

Jakob Huber [ORCID] · **Jonas Vogler** · **Ewald Werner**

Multiscale modeling of the mechanical behavior of brazed Ni-based superalloy sheet metals

Abstract The elastic–plastic behavior of brazed Ni-based superalloys used in abradable turbomachinery sealing systems is analyzed by means of numerical simulations. A sequential multiscale modeling approach is employed to analyze the relevant effects on the mechanical behavior of a layered composite consisting of the braze metal and the joining partners. The focus of the investigations lies on the role of the multiphase microstructure within the brazing layer and the significance of microscopic parameters such as, for example, the volume fraction of the phases compared to macroscopic parameters (e.g., the brazing layer thickness). A representative volume element is employed on the microscale, and a layered composite is modeled on the macroscale to capture all relevant effects on both length scales during mechanical loading of the layered material composite. Virtual tensile tests at different temperatures and strain rates are chosen as a controlled testing environment that captures the characteristic loading conditions during a rubbing event in a turbomachinery. The parameter on the microscale with the highest influence on the mechanical behavior is the volume ratio of the brittle and ductile phases. It also has a significant effect on the macroscopic mechanical behavior. To reduce the risk of damage, it is advised to minimize the fraction of brittle phases in the brazing layer. According to the simulation results, this can be even more effective than reducing the overall thickness of the brazing layer. Additionally, an improvement of an existing analytical model for the estimation of the flow stress in the ductile phase of a dual-phase microstructure is proposed. By increasing the order of the root function in the analytic model, the effect of stress distribution between brittle and ductile phases can be incorporated in an empirical manner. This reduces the deviation between the analytical and the numerical approaches significantly.

Keywords Brazed Ni-based superalloy · Crystal plasticity · Micro-damage · Abradable sealing systems · Multiscale modeling · Virtual laboratory

1 Introduction

1.1 Motivation and current state of research

Ni-based brazing metals are commonly used for joining and repairing Ni-based superalloys used in high-temperature applications. Besides providing a joint that is resistant to high temperatures, the brazing layers

J. Huber (✉)· E. Werner
Institute of Materials Science and Mechanics of Materials, Technical University of Munich, Boltzmannstraße 15, 85748 Garching, Germany
E-mail: jakobmartin.huber@tum.de

J. Vogler
Chair for Metals and Alloys, University of Bayreuth, Prof.-Rüdiger-Bormann-Str. 1, 95447 Bayreuth, Germany

formed in the joining process can also deteriorate the mechanical properties of the material composite. An example where the brazing process has a particularly detrimental effect is abradable sealing systems in a turbomachinery. Honeycomb liners are typically brazed to a carrier plate and form the stator of the sealing system. Sealing fins attached to the rotor rub into the honeycomb liners either in order to achieve a minimal leakage air flow or due to a change of the operation conditions [1]. Due to capillary action, the brazing material can rise from the carrier plate up to the rubbing surface and form a layered composite consisting of the base metal and the braze filler metal (see Fig. 1, left). Brittle phases that form during brazing pose a high risk of rotor damage as they show strong mechanical resistance up to high temperatures. Additionally, brittle phases can act as an accelerator for critical stator damage such as cracking and large breakouts in the honeycomb liners, which can significantly increase the leakage flow and can also damage other parts of the turbomachinery.

The microstructure of the brazing layer between the joining partners shows different characteristics depending on the duration of brazing and the braze gap size [2–4]. A common feature is the coexistence of brittle and ductile phases in the brazing zone. Ulan kyzy et al. [5] identified three major microstructural constituents in the double-foiled segments of a Hastelloy X honeycomb liner brazed with BNi-5 filler metal. Those were a matrix of γ-nickel solid solution (1), NiSi (2) and several silicides of $Ni_y(Cr,Mo)_x Si$ type (3). A similar microstructure could be identified in Haynes 214 sheet metals brazed with BNi-5 (see contrast of back-scattered electrons in Fig. 1, right). Previous studies compared Hastelloy X with Haynes 214 as honeycomb liner materials [6,7]. It was shown that the latter alloy leads to higher mechanical and thermal loads on the rotor during a rubbing event. For this reason, we focus on Haynes 214 instead of Hastelloy X in this study.

According to Hawk et al. [3], the matrix (1) has a microstructure similar to the base metal Haynes 214 consisting of γ-nickel and nanometer-sized γ'-precipitates. Measurements of microhardness showed a strong local increase in hardness in the Si-rich phase (2) and the silicides (3) [3,5]. Table 1 shows the chemical composition of two base metals typically used for the honeycomb foils as well as the braze metal BNi-5.

Since in the literature mainly macroscopic mechanical testing has been performed as, e.g., by Hawk et al. [3] as well as by Li and Schulson [8], the effect of the microstructure on the mechanical behavior of brazed joints is not fully understood. Isolated mechanical testing of the identified phases is cumbersome due to the difficulty of capturing the conditions in the brazing layer that stem from the process of brazing. Numerical simulations can help to overcome this challenge. However, current modeling approaches treat the brazing
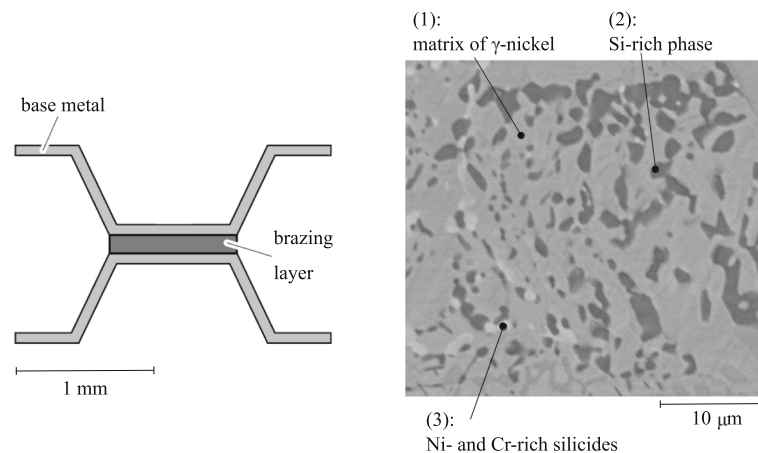

Fig. 1 Left: schematic top view of a honeycomb double-foiled segment with capillary braze, right: exemplary microstructure (contrast of back-scattered electrons) of the brazing layer in a honeycomb double-foiled segment with phases similar to those identified by Ulan kyzy et al. [5] for brazed Hastelloy X sheets

Table 1 Chemical composition of two common base metals used for honeycomb foils as well as the braze metal BNi-5 in mass-%, balance is nickel [5]

Alloy	Cr	Fe	Mo	W	Mn	Al	Si	Co	Cu
Hastelloy X	21.70	19.73	8.44	0.68	0.64	0.07	0.35	0.79	0.35
Haynes 214	16.70	3.71	0.10	–	0.41	4.46	0.04	0.01	–
BNi-5	19.00	–	–	–	–	–	10.00	–	–

zone as either purely ductile or purely brittle depicted by an elastic material behavior while neglecting the multiphase microstructure in the brazing layer [7,9].

1.2 Scope and goals of this work

In this work, numerical simulations are conducted to identify the most influential effects on the elastic–plastic behavior of the layered composite on the macroscale as well as on the microscale. The Ni-based superalloy Haynes 214 is chosen as base metal and BNi-5 as braze filler metal. Virtual high-temperature tensile tests at different strain rates will serve as a model basis for the simulative studies. They depict the characteristics of the loading conditions during a rubbing event in a controlled environment that will allow a quantitative comparison between the simulations and future experiments.

The goal of this work is twofold. First, the necessary depth of modeling and crucial parameters for experimental characterization of brazed Ni-based sheet metals are identified and validated. Second, guidelines for a beneficial microstructure as well as a beneficial macroscopic geometry of base metal-braze composites in honeycomb liners will be derived. In particular, this means

1. lowering the resistance against the rubbing partner by reducing the yield limit as well as strain hardening, and
2. decreasing the risk of critical damage in the honeycomb liner by lowering stress peaks on both the microscale and the macroscale considering the type and location of damage.

This work is organized as follows: In Sect. 2, the constitutive relations employed on each scale are described. A sequential multiscale simulation setup is presented in Sect. 3. The employed micromechanical model is validated with experimental results from the literature in Sect. 4. Sensitivity studies on both scales are discussed in Sect. 5. The work is closed in Sect. 6 with the most important conclusions as well as an outlook on further studies.

2 Constitutive models used on different scales

On each scale, the relevant mechanisms influencing the mechanical material behavior should be incorporated. In order to capture the effective material behavior and to assess potential micro-damage, the brazing layer is microstructurally resolved. The base metal is only considered on the macroscale as an isotropic elastic–plastic material with its uniaxial flow curve taken directly from experiment [10].

2.1 Microscale

A phenomenological elastic–viscoplastic material law considering the face-centered cubic (fcc) crystal structure is used for the ductile nickel solid solution phase (1). The generalized Hooke's law is used to calculate the second Piola–Kirchhoff stress tensor in the plastic configuration $\mathbf{S}_p$ caused by elastic deformation $\mathbf{F}_e$ depicted by the Green–Lagrange strain tensor $\mathbf{E} = 1/2(\mathbf{F}_e^T \mathbf{F}_e - \mathbf{I})$ with $\mathbf{I}$ being the second rank identity tensor,

$$\mathbf{S}_p = \mathbb{C} : \mathbf{E}. \tag{1}$$

In Eq. (1), $\mathbb{C}$ is the fourth-order elastic stiffness tensor inheriting the symmetries of the underlying crystal lattice. For the cubic crystal of the nickel solid solution phase, three independent elastic constants are required (C_{11}, C_{12} and C_{44}) [11]. In the framework of large deformations, the total deformation gradient $\mathbf{F}$ is multiplicatively split into a lattice-preserving plastic deformation step followed by a lattice distorting elastic deformation step, $\mathbf{F} = \mathbf{F}_e \mathbf{F}_p$. Plastic deformation is depicted by the plastic deformation gradient $\mathbf{F}_p$. Its evolution is given by the single dot product of the plastic velocity gradient $\mathbf{L}_p$ and the plastic deformation gradient

$$\dot{\mathbf{F}}_p = \mathbf{L}_p \mathbf{F}_p. \tag{2}$$

For crystal plasticity, it is assumed that the plastic deformation follows the slip systems of the underlying crystal lattice. A suitable flow rule for a fcc crystal lattice can be formulated as:

$$\mathbf{L}_p = \sum_{\alpha=1}^{12} \dot{\gamma}^\alpha \mathbf{m}^\alpha \otimes \mathbf{n}^\alpha, \tag{3}$$

Table 2 Parameters of the constitutive laws used on the microscale at room temperature (20 °C) and close to the melting point (1100 °C)

Parameter	$T = 20\,°C$	$T = 1100\,°C$
Ductile phase—crystal elasticity		
C_{11} [GPa]	245	180
C_{12} [GPa]	150	120
C_{44} [GPa]	124	73
Ductile phase—crystal plasticity		
a [−]	1.75	1.75
$\dot{\gamma}_0$ [s^{-1}]	0.4	0.4
h_0 [MPa]	1000	1000
n [−]	15	4.2
τ_c [MPa]	$220 + \frac{k_c}{\sqrt{d}}$	55
τ_∞ [MPa]	$416 + \frac{k_\infty}{\sqrt{d}}$	163
Brittle phases—isotropic linear elasticity		
E [GPa]	220	140
ν [−]	0.31	0.34

with the slip direction $\mathbf{m}^\alpha$ and the normal of the slip plane $\mathbf{n}^\alpha$ defining the slip system α [12]. The shear rate of plastic deformation $\dot{\gamma}^\alpha$ in the slip system α caused by the Schmid shear stress $\tau^\alpha = \mathbf{S}_p : \mathbf{m}^\alpha \otimes \mathbf{n}^\alpha$ is calculated using a phenomenological power law by Rice, Hutchinson and Peirce [13]

$$\dot{\gamma}^\alpha = \dot{\gamma}_0^\alpha \left| \frac{\tau^\alpha}{\tau_c^\alpha} \right|^n \; \mathrm{sgn}\left(\tau^\alpha\right). \tag{4}$$

Therein a reference shear rate $\dot{\gamma}_0^\alpha$ acts as a proportional factor on the ratio of the Schmid shear stress acting on the slip system α and the corresponding critical resolved shear stress τ_c^α. The evolution of the critical resolved shear stress is given as:

$$\dot{\tau}_c^\alpha = \sum_{\alpha'=1}^{12} h_{\alpha\alpha'} \left| \dot{\gamma}^{\alpha'} \right|, \tag{5}$$

where $h_{\alpha\alpha'}$ is a hardening matrix accounting for active and latent hardening

$$h_{\alpha\alpha'} = q_{\alpha\alpha'} h_0 \left| 1 - \frac{\tau_c^{\alpha'}}{\tau_\infty} \right|^a \mathrm{sgn}\left(1 - \frac{\tau_c^{\alpha'}}{\tau_\infty} \right). \tag{6}$$

In the equation above h_0, a and τ_∞ are hardening parameters and $q_{\alpha\alpha'}$ assigns a factor of 1.0 for coplanar slip systems and 1.4 for systems with distinct slip planes. For the fcc crystal structure, the hardening parameters are assumed to be the same for all 12 slip systems [12].

The corresponding material parameters for Haynes 214 have been identified by Fischer et al. [6] by comparing experimental tensile tests at different strain rates with virtual tensile tests on a polycrystalline representative volume element (RVE). According to Jamaloei et al. [4], Ni$_3$Si precipitates can be found in the ductile phase of the brazing layer. These precipitates show the same crystal structure as the γ' phase of Haynes 214 and have a similar size as the γ' precipitates. Therefore, the already identified material parameters of Haynes 214 should be suitable for the ductile phase in the brazing layer. The crystal elastic constants were chosen to match not only the effective Young's modulus E and Poisson's ratio ν but also to achieve a single crystal anisotropy factor typical for a Ni-based alloy (Zener ratio of $A = 2.4$) [14]. This is an enhancement to [6] in which the elastic anisotropy of the grains is neglected.

The remaining phases (phases 2 and 3 in Fig. 1) are assumed as purely brittle. As a first approach, a purely isotropic linear elastic material behavior that matches the effective elastic properties of polycrystalline Haynes 214 [15] is assigned to the brittle phases. Table 2 summarizes the material parameters used for the ductile and brittle phases at room temperature ($T = 20\,°C$) as well as at $T = 1100\,°C$ which is close to the melting point of Haynes 214 ($T_{melt} = 1355\,°C$).

2.2 Macroscale

The most important effects on the macroscale are expected to be the temperature and rate dependencies of the elastic–plastic material behavior. A preliminary study considering fully resolved grains assigned with crystal elastic–plastic material behavior has been conducted to analyze the influence of varying crystal orientations on the base metal layers. It was shown that the stress heterogeneity due to the contrast between ductile and brittle layers is a magnitude of order larger than the stress heterogeneity due to the contrast between differently orientated grains in the base metal. Therefore, the crystalline structure of the base metal can be regarded as a second-order effect on the fluctuations of mechanical fields in the layered composite. Consequently, the base metal can be regarded as homogeneous and isotropic. A further study on the propagation of microstructural variation to the macroscopic material behavior showed that also the brazing layer can be regarded as homogeneous and isotropic (see Sect. 3.1). These considerations lead to the macroscopic material behavior of the base metal-braze layered composite being modeled as follows:

- Homogeneous material in each layer,
- Isotropic elastic–plastic material with von Mises yield criterion and isotropic hardening, and
- Strain rate dependency of the yield surface.

All necessary material parameters for the base metal are taken from tensile tests conducted at different strain rates by Ulan kyzy [10]. For the brazing layer, a homogenization approach using a dual-phase RVE is employed (see Sect. 3.1). The uniaxial yield limit at different levels of plastic equivalent strain and strain rate is given as tabular data to the FE-solver Abaqus [16].

3 Multiscale simulation setup for virtual tensile tests

3.1 Representative volume element of the microstructure in a brazing layer

On the microscale the focus lies on capturing the relevant effects of the multiphase microstructure consisting of brittle and ductile phases. To model the effect of the anisotropic flow behavior of the grains in the ductile phase, the above-described crystal elastic–plastic constitutive law is employed. Compared to modeling isotropic phases (as done by, for example, [17,18]), additional contributions to the stress and strain fluctuations due to crystallographic misorientation can be depicted. This is potentially important for assessing the potential risk of micro-damage.

A fully periodic RVE is used to model the microstructure of the brazing layer in a highly resolved manner. A necessary condition in the concept of the RVE is the separation of scales [19], which can be formulated as

$$L_{\mathrm{h}} \ << \ L_{\mathrm{RVE}} \ << \ L_{\mathrm{macro}}. \tag{7}$$

In the microstructure of the brazing layer, the characteristic length of the heterogeneity L_{h} is the diameter of the smallest silicides (3 in Fig. 1). The macroscopic length scale L_{macro} is set to be the brazing layer thickness t_{braze}, which lies in the range of 50 μm to 150 μm. For the generation of the geometry of the RVE, the software Neper is employed [20]. The implemented grain growth algorithm is used which is based on a Laguerre–Voronoï tessellation and lets the user introduce statistics for the grains' equivalent diameter (diameter d of a sphere with same volume as the grain) and shape. In order to account for differently sized grains, the grain diameter is set to lie in the range $L_{\mathrm{h}} = [0.5 - -2.0]$ μm. The grains' equivalent diameter follows a logarithmic normal distribution (mean value of 0.87 μm and standard deviation of 0.3 μm). This logarithmic normal distribution was chosen as it is generally able to describe measured grain size distributions as shown by, for example, [21] and allows for a few larger precipitates that were also observed, even though those were of small quantity. Through a "coloring" process in which one out of two phases is assigned to each grain the RVE is divided into a brittle and a ductile phase. Thereby, the grains can be grouped to form a bigger microstructural cluster. The coloring process is random with the fraction of the ductile phase being the only condition that has to be satisfied. In combination with the varying grain diameter, a wide range of microstructural cluster sizes and shapes can be achieved. Compared to a multilevel tessellation [22], this approach has the advantage that the internal boundaries in a single phase are conserved. This is relevant for the ductile phase wherein varying crystallographic orientations depict a possible source of heterogeneity inside a single phase. In this approach, the grain size dependency of the flow stress (Hall–Petch relation) is not transferred to the grains individually as suggested by Meier et al. [23] or Fischer et al. [6]. Instead, the critical resolved shear stress
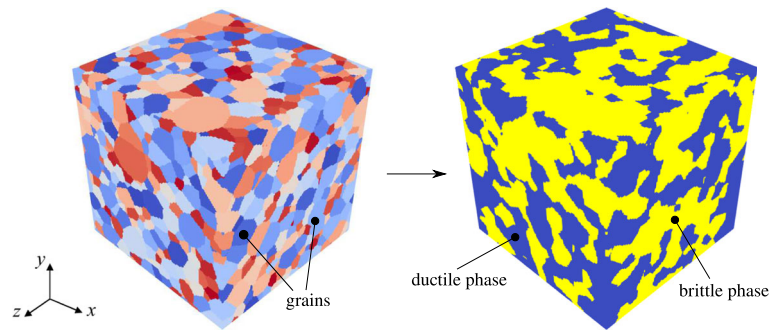
Fig. 2 Grain to phase assignment. Laguerre–Voronoï tessellation with varying grain size (left), colored RVE depicting a dual-phase microstructure (right)

τ_c and the saturation stress τ_∞ are chosen to be the same for all grains in the ductile phase, and their values are set according to the mean equivalent grain diameter using the Hall–Petch constants k_c and k_∞ from [7]. It is assumed that the geometrically necessary plastic deformation at the grain boundaries depicted by a spatial jump in the crystallographic orientation in combination with the hardening behavior following the equations (5) and (6) already accounts for a varying resistance against dislocation slip for grains with distinct sizes. Smaller grains have a higher proportion of areas of geometrically necessary deformation than bigger grains and therefore exhibit a higher mean flow stress. A shortcoming of this approach is that the contrast of the flow stress between two differently sized grains only builds up gradually with progressing deformation but is not present at the initial plastic deformation. As the mechanical contrast between the brittle and ductile phases is expected to be much higher than the contrast between grains of the ductile phase due to distinct grain sizes, the above-mentioned shortcoming is accepted in order to reduce the implementation effort. At this point, it should also be noted that the grain size hardening is only applicable to polycrystals up the recrystallization temperature ($T/T_{\text{melt}} < 0.3$–0.5) [24]. For the elevated temperatures ($T = 1100\,°C$) considered in this work, the grain size effect is assumed to be insignificant and is therefore neglected (see Table 2).

The geometric tessellation consists of 2000 grains. This is a rather large number of grains compared to studies by other authors [9,17] who employed RVEs consisting of only 150 grains. However, regarding the complex microstructural clusters showing features of different size this is necessary to ensure the representativeness of the volume element. Figure 2 shows the Laguerre–Voronoï tessellation with varying grain sizes as well as the colored RVE showing the dual-phase microstructure with a fraction of ductile phases of $P_{\text{ductile}} = 0.50$.

Due to its superior computational performance for fully periodic solution fields, a spectral method for solving mechanical equilibrium is employed on the microscale. The RVE is discretized by 128 voxels in each spatial direction. A convergence study that justifies this numerical resolution can be found in "Appendix B". The spectral method implemented in the simulation toolkit DAMASK [12] was verified against a FEM simulation. This was done for the case of the high contrast in the numerical tangential stiffness between the purely elastic brittle and the yielding ductile phases. This characteristic of the microstructure in the brazing layer is challenging for the spectral solver due to jumps in the stress field at phase boundaries. Both solution methods showed good agreement, and the spectral solver is considered to be suitable for the microstructures that are observed in the honeycomb brazing layer. The micromechanical model itself was validated with an experimental analysis of a similar microstructure taken from the literature (see Sect. 4).

In order to assess the significance of microstructural variation influencing the mechanical behavior on the macroscale, virtual uniaxial tensile tests were performed on different microstructures. Concerning the mechanical model on the macroscale (see Sect. 3.2), it is important to evaluate whether the effective material parameters show significant uncertainties leading to a potentially heterogeneous and anisotropic material behavior in the brazing layer on the macroscale. The tests were carried out at room temperature and under quasi-static conditions. As a measure for the uncertainties on the macroscale due to variations in the microstructure, the coefficient of variation CV is introduced as the ratio of the standard deviation to the mean value of the mechanical response of the RVE

$$\text{CV} = \frac{\text{Standard deviation}}{\text{Mean value}}. \tag{8}$$

Two types of microstructural variation were analyzed. The first one was the variation due to different phase morphology. A random grain-to-phase-assignment process was applied to generate 10 different microstructures
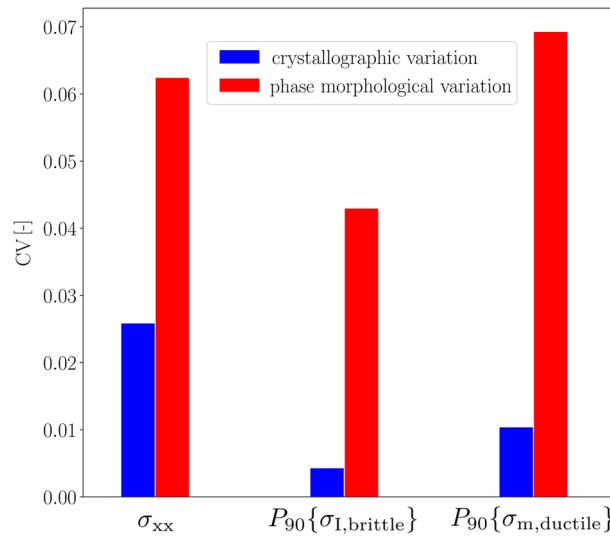
Fig. 3 Coefficient of variation (CV) for different stress measures at a volume average strain of $\bar{\varepsilon} = 5.0\%$

with a fraction of the ductile phase of $P_{\text{ductile}} = 0.50$. The second type of microstructural variation concerns the crystallographic orientation of the grains of the ductile phase. As extreme case all grains of the ductile phase were given the same crystallographic orientation. This represents a single-crystalline ductile phase. The loading direction was then successively orientated parallel to three different crystallographic directions, the first one being [100], the second one [110] and the third one [111]. This was realized by first aligning the crystal coordinate system with the laboratory system and then either no further rotation (1), a rotation of 45° about the y-axis (2) or a rotation of 45° about the y-axis followed by a rotation of 35.3° about the z-axis (3). For the two types of microstructural variation, the CV of the mechanical response at 5% volume-averaged strain is shown in Fig. 3.

The stress measures evaluated are the stress component in the load direction σ_{xx} as well as the 90% quantiles of the first principal stress in the brittle phases $P_{90}\{\sigma_{\text{I,brittle}}\}$ and the hydrostatic stress in the ductile phase $P_{90}\{\sigma_{\text{m,ductile}}\}$. The CV is small for both types of microstructural variation. For a varying phase morphology, the mechanical response of the RVE varies stronger than for the varied crystallographic texture, but the CV is still less than 7%. The chosen fraction of the ductile phase of $P_{\text{ductile}} = 0.50$ is expected to form the most complex grain clusters and subsequently the strongest possible morphological variation. Regarding the crystallographic variation, it is expected that an increasing fraction of the ductile phase could increase the microstructural variation further to a certain degree. However, since the observed effect of crystallographic variation on the stress measures of interest is significantly smaller than the effect of the morphological variation, any potential increase in the CV is expected to be negligible. Therefore, an assumption of isotropic and homogeneous material behavior in the brazing layer on the macroscale is reasonable as long as the volume fraction of the ductile phase is constant.

3.2 Macroscopic model of the layered composite

The macroscopic tensile sample is modeled as a layered composite of thickness t_{comp} with a brazing layer that shows spatial thickness fluctuations. This is motivated by the observation that the depth of interdiffusion varies along the in-plane directions forming a non-flat interface between the brazing layer and the base sheet metal. The layers are generated by coloring a Voronoï tessellation with 2000 equally sized cells on the macroscale according to the cell centroid positions, which leads to an interface roughness in the order of magnitude of the Voronoï cell diameter. Figure 4 shows the procedure schematically. As a model input parameter, the mean thickness of the brazing layer t_{braze} is used.

The interface roughness is smaller than the sample's in-plane dimensions by a factor of approximately 12. Therefore, the condition of the separation of scales is satisfied, and a semi-periodic macroscopic RVE with periodic boundary conditions applied in the x- and z-directions is employed to reduce the computational time significantly. For the y-direction force free surface boundary conditions are applied. The uniaxial tensile load
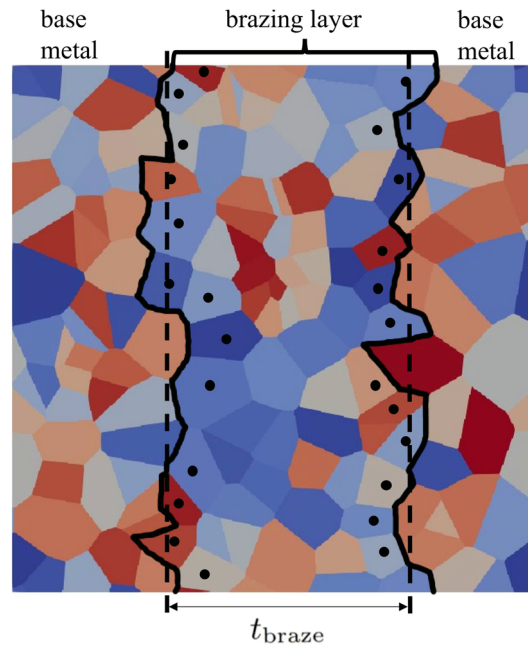
Fig. 4 Generation of a layered composite with rough interfaces between base metal and brazing layer, the dashed lines indicate the spatial criterion for material assignment to the Voronoï cells based on the centroid positions
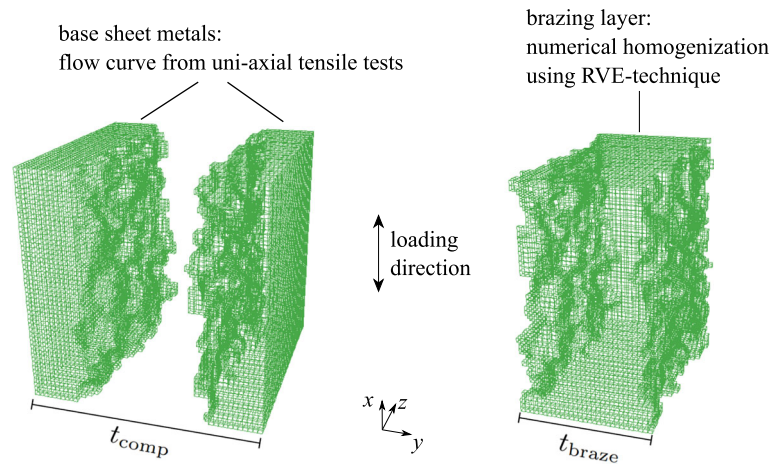

Fig. 5 Macroscopic model of the layered composite and methods to derive the material behavior for each layer. Base sheet metals (left) and brazing layer (right) $t_{\text{braze}} = 0.5\, t_{\text{comp}}$

is introduced over a multipoint constraint that prescribes a volume-averaged deformation in the x-direction. Details of the implementation of periodic boundary conditions can be found in, for example, [25]. The cube-shaped computational domain is discretized by 65^3 brick finite elements with linear shape functions (C3D8R). An example of the layered composite model with a mean thickness of the brazing layer of $t_{\text{braze}} = 0.5\, t_{\text{comp}}$ is provided in Fig. 5 together with the sources of the material behavior for each layer that are described in Sect. 2. To be able to deal with the free surfaces in the y-direction of the tensile samples, the finite element method is chosen as the solution method for mechanical equilibrium on the macroscale. This modeling approach still accounts for an accurate representation of the interface between the base metal and the brazing layer while neglecting second-order effects caused by anisotropic material behavior of the oligocrystalline base sheet metals. A summary of the reference configuration in terms of geometry and loading for the simulations on the microscale as well as the macroscale is given in "Appendix C". The values reported there are used if not stated differently.
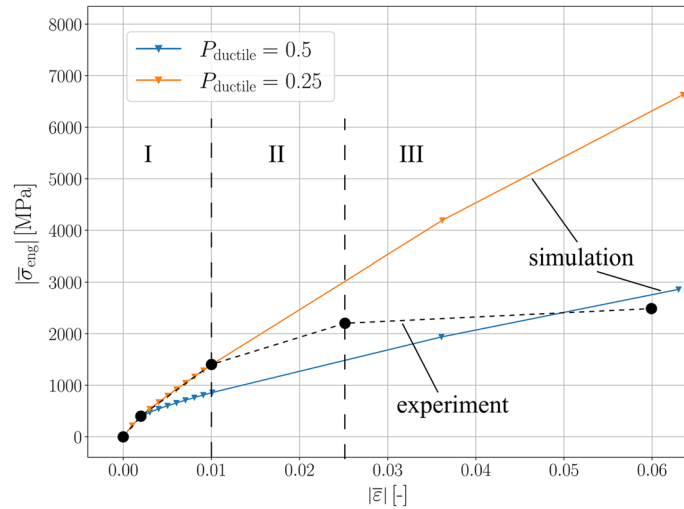
Fig. 6 Comparison of simulation and experiment [8] in terms of engineering stress–strain curves for uniaxial compression. The segments on the strain axis indicate regimes of distinct degrees of accordance between simulation and experiment

4 Validation of the microscopic model

Li et al. [8] experimentally analyzed the mechanical properties of a nickel silicide similar to the silicides in the brazing layer of the honeycombs (phases 2 and 3 in Fig. 1). The brittle silicide matrix was enhanced with ductile particles. Those particles consisted of nickel solid solution with Ni_3Si precipitates. The precipitates have a similar size and the same crystallographic structure [26] as the γ' precipitates in Haynes 214. A very similar microstructure is also found in the brazing layer of honeycomb double-foiled segments. Therefore, the mechanical tests conducted by Li et al. [8] are suitable for validating the micromechanical model. In the experiment, the ductile particles were encased by Ni_3Si rims. It is not clarified if these rims show a brittle or ductile behavior. Their hardness lies between the hardness of the brittle matrix and the ductile particles but is closer to the hardness of the brittle matrix. Therefore, in the simulation model the bounding cases of purely brittle and purely ductile rims are both considered, which leads to a fraction of the ductile phase of $P_{ductile} = 0.25$ and $P_{ductile} = 0.5$, respectively. The comparison of the volume-averaged stress–strain curves between simulation and experiment (Fig. 6) shows a good agreement regarding the bounds in the fraction of the ductile phase. Three segments on the volume-averaged strain axis can be distinguished. For elastic deformation and small plastic strains (I) the experimental results almost coincide with the simulation results assuming purely brittle rims ($P_{ductile} = 0.25$). With increasing plastic deformation, the stress response is overestimated by the simulation, but the stress value as well as the hardening slope remains in the bounds given by the simulation (II). At approximately 2.5% volume-averaged strain, the hardening slope falls below the lower bound, and at approximately 5% volume-averaged strain also the stress response falls out of the given bounds (III). This deviation could partly be explained by the increased hardness of the Ni_3Si rims. The onset of plastic deformation in the rims would give additional contributions to the volume-averaged deformation at higher stresses. However, this effect can explain the behavior not further than up to segment II. Regarding the drastic decrease of the hardening slope in segment III, there has to be an additional source of inelastic deformation which is possibly micro-damage. This hypothesis is in accordance with the observation of micro-cracks in the brittle matrix at rather small strains $\bar{\varepsilon} = 2.3\%$ reported by Li et al. [8].

## 5 Sensitivity studies on the micro- and the macroscale

In order to obtain a better understanding of the constitutive behavior of the brazing layer, sensitivity studies are conducted on the microscale. The flow curves extracted from the micromechanical simulations will be incorporated in the material behavior used for the macroscopic studies.

### 5.1 Behavior of the brazing layer on the microscale

5.1.1 Flow behavior in dependency of the volume fraction of the ductile phase

According to Hawk et al. [3], the fractions of brittle and ductile phases depend significantly on brazing parameters such as brazing temperature and duration. Therefore, a wide range of possible phase fractions has to be considered. Figure 7a shows the volume-averaged stress–strain curves for five different fractions of ductile and brittle phases. A strong influence of the phase fraction is apparent. For a decreasing fraction of the ductile phase, the hardening of the dual-phase microstructure increases following a nonlinear rule of mixture. As we do not yet have a quantitative criterion for damage initiation, the validity limit of the micromechanical model is drawn into the stress–strain curves in Fig. 7a. The limit is an estimate of the maximal stress and strain based on the experimental findings of Li et al. [8] who observed a fracture stress of approximately $\overline{\sigma}_{max} = 2400\,\mathrm{MPa}$ and a fracture strain of approximately $\overline{\varepsilon}_{max} = 0.025$. Taking the first principal stress in the brittle phase as a failure criterion, one obtains an estimate of the maximum volume-averaged stresses and strains that are possible. In this estimate of the validity limit, it is assumed that the micro-damage starts in the brittle phases at the micro-stress level that leads to the failure in the microstructures used for validation ($P_{ductile} = 0.375$). For an increasing fraction of the ductile phase, the failure criterion has to be extended in a way that it incorporates the failure of the ductile phase as well.

Looking at the yield limit in dependency of the fraction of the ductile phase (Fig. 7b), one can observe that for microstructures dominated by the brittle phases ($P_{ductile} < 0.5$) the hardening slope increases progressively following a strongly nonlinear rule of mixture. However, the initial yield point is hardly dependent on the fraction of the ductile phase. This behavior was already predicted by Fischmeister and Karlsson [27] for dual-phase microstructures that show negligible phase contrast in the purely elastic regime and can be verified when reducing the amount of plastic strain used for the definition of the yield limit R_p successively (see Fig. 7b).
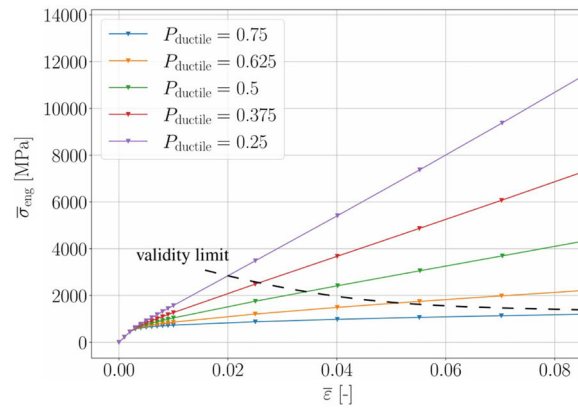
(a) Engineering stress strain curves with validity limit of the micromechanical model.
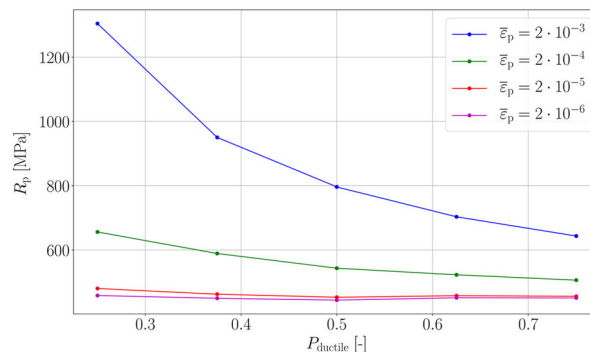
(b) Initial yield limit of aggregate for different volume averaged plastic strains $\overline{\varepsilon}_p$.

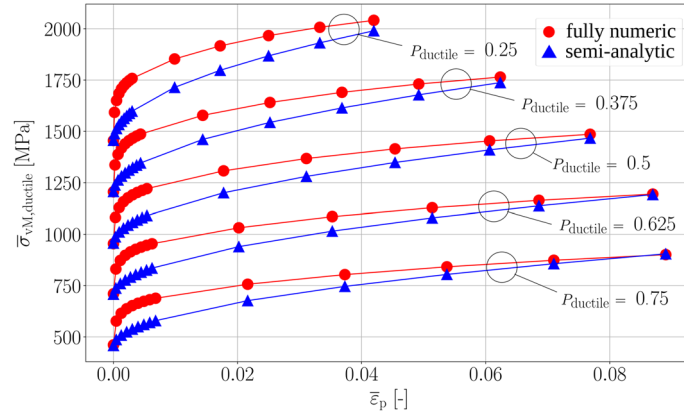**Fig. 7** Flow behavior of the brazing layer for varying fractions of the ductile phase

Fig. 8 Comparison of fully numerical RVE simulations and a semianalytical approach using the equation proposed by [28] for which phase-specific deformations are taken from the RVE simulations. Volume-averaged von Mises stress in the ductile phase containing a hard second phase plotted over plastic strain of whole aggregate. For better readability, a successive offset of 250 MPa in the stress axis is employed for each phase fraction starting from $P_{\text{ductile}} = 0.75$

At this point, it should be remembered that there is some heterogeneity in the ductile phase due to the crystal elastic anisotropy of the nickel solid solution phase. Therefore, there is also a small contrast between the phases in terms of their elastic behavior. However, according to the simulation results this contrast is not sufficient for a noticeable dependency of the initial yield point on the fraction of the ductile phase.

Fischmeister and Karlsson [27] suggested a model for the estimation of the flow stress of a soft matrix including a hard second phase. Therefore, this model can be used to verify the inverse case to a brittle matrix containing ductile particles that is analyzed in Sect. 4. The estimation is based on the hardening of the material by means of geometrically necessary dislocations (GNDs) at grain boundaries in the matrix as well as at phase boundaries. In the presented case, the soft phase is the ductile nickel solid solution and the hard phase are the brittle silicides. The flow stress of the soft phase containing a hard second phase can then be derived as:

$$\bar{\sigma}_{\text{ductile}} = \sigma_{\text{r,ductile}} + CG \cdot \sqrt{\frac{b\bar{\varepsilon}}{\lambda_{\text{ductile}}}} \cdot \sqrt{1 + \frac{P_{\text{brittle}}}{P_{\text{ductile}}} \cdot \frac{\bar{\varepsilon} - \bar{\varepsilon}_{\text{brittle}}}{\bar{\varepsilon}}}. \tag{9}$$

In this equation, the friction stress $\sigma_{\text{r,ductile}}$, the collecting constant C (for details, see [28]), the shear modulus G and the magnitude of the Burgers vector b are constants. As we do not alter the average grain size in the ductile phase when varying the fraction of the ductile phase, the mean free path for dislocation slip λ_{ductile} is also constant. This means that the flow stress in the ductile phase is a function of only the volume-averaged strain of the whole aggregate $\bar{\varepsilon}$, the averaged strain of the brittle phases $\bar{\varepsilon}_{\text{brittle}}$ and the ratio of the phase fractions $\frac{P_{\text{brittle}}}{P_{\text{ductile}}}$. As Fischmeister considers GNDs inside the soft phase while assuming a purely elastic deformation in the hard phase his model is well applicable to the presented microstructure. Figure 8 compares the flow stress in the ductile phase extracted directly from the RVE simulations with the flow stress in the ductile phase calculated by Eq. (9). The difference in averaged strain between the aggregate and the brittle phases is taken from the RVE simulations. Both approaches show a similar trend of the flow stress of the ductile phase with increasing deformation as well as varying fractions of the ductile phase. However, the initial hardening of the ductile phase is underestimated by Eq. (9) for small strains. In contrast, for larger strains the semi-analytic approach overestimates the amount of hardening.

A possible mechanism that most likely should be incorporated to explain this mismatch is the redistribution of stress from the ductile to the brittle phases. One can indeed verify this by plotting the ratio of the volume-averaged von Mises stress in the brittle and ductile phases over the averaged plastic strain (see Fig. 9). For a decreasing fraction of the ductile phase, the accordance deteriorates. This is to be expected as the assumption of a continuous ductile matrix becomes increasingly violated which is also clear when inspecting Fig. 9. The effect of stress redistribution from the ductile to the brittle phases becomes significantly stronger for a decreasing fraction of the ductile phase. In the limit case, a brittle matrix impedes the plastic deformation of the ductile phase. An empirical modification of Eq. (9) to reduce the mismatch between the two approaches is given in "Appendix D".
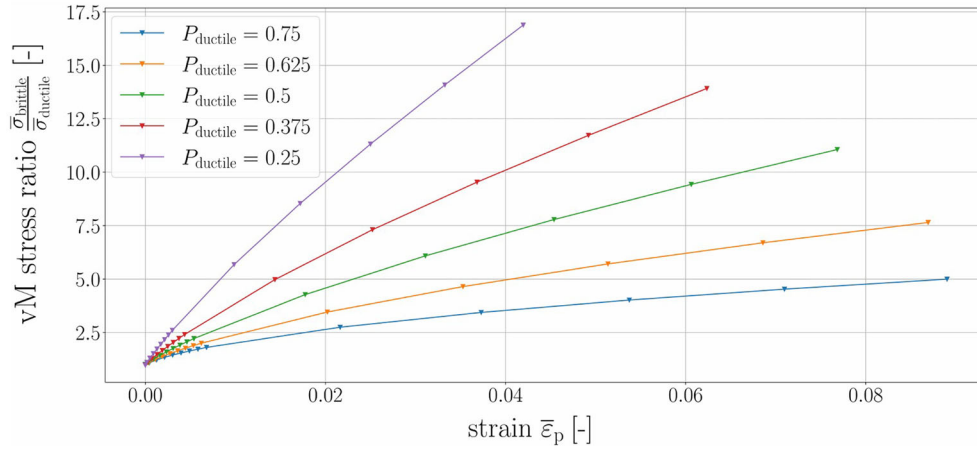
Fig. 9 Ratio of the volume-averaged von Mises stress over the volume-averaged plastic strain of the aggregate for five fractions of the ductile phase
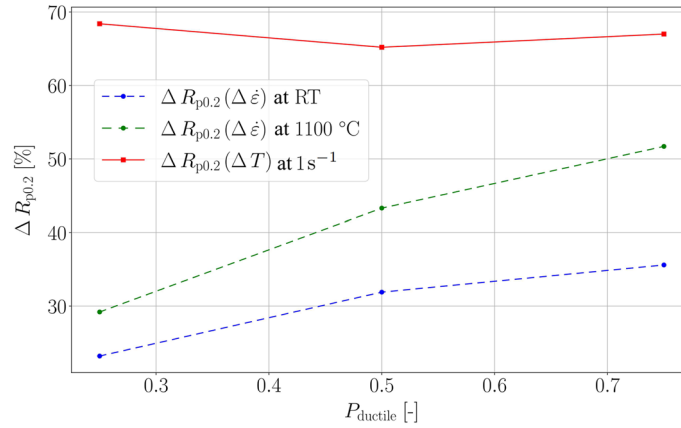

Fig. 10 Difference in the yield limit between the extreme values in temperature (20 vs. 1100 °C) and between the extreme values in strain rate (1 vs. 50 s^{-1}) for three different fractions of the ductile phase

5.1.2 Strain rate and temperature dependency of the flow behavior

As two important material properties for the analysis of rubbing events, the strain rate as well as the temperature dependency of the initial flow behavior are investigated for different fractions of the ductile phase. The positive relative difference in the yield limit for the extremes in the strain rate or the temperature is evaluated as:

$$\Delta R_{p0.2} = \frac{R_{p0.2}^{max} - R_{p0.2}^{min}}{R_{p0.2}^{max}}, \tag{10}$$

where $R_{p0.2}^{max}$ corresponds to the maximum value of the strain rate or the minimum value of the temperature and $R_{p0.2}^{min}$ corresponds to the minimum value of the strain rate or the maximum value of the temperature.

As can be seen in Fig. 10, the temperature dependency of the initial yield limit is hardly influenced by the fraction of the ductile phase. The reason for this observation could be found in the temperature-dependent material behavior of the single phases. The ductile phase shows a temperature dependency in the elastic constants as well as in the yield limit in the form of thermal softening. Therefore, it might be expected that the temperature dependency of the dual-phase microstructure rises in its magnitude with an increasing fraction of the ductile phase. However, this is not the case as the brittle phases also show a temperature dependency in their elastic constants.
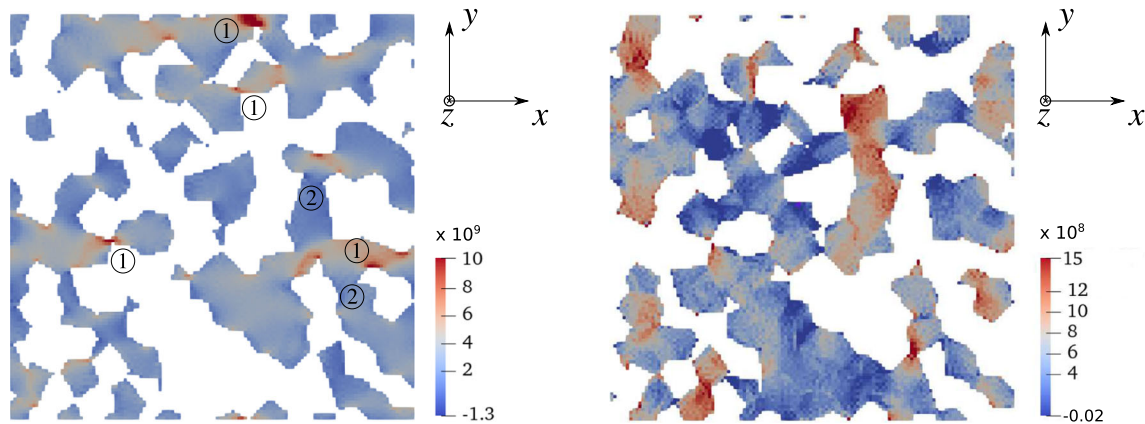
Fig. 11 Stress fields [Pa] for uniaxial tension in the x-direction at $\bar{\varepsilon} = 2.5\%$ and $P_{\text{ductile}} = 0.5$. First principal stress in the brittle phases (left) and hydrostatic stress in the ductile phase (right)

5.1.3 Assessment of the risk of micro-damage

According to experimental observations, micro-damage is assumed to occur first in the brittle phases [8]. However, the stress state in the ductile phase should also be monitored since the experimental observations also show small areas of the fracture surface that indicate ductile material failure. The risk of damage in the brittle phases can be assessed in terms of the first principal stress according to the Rankine criterion [29]. In the ductile phase, the hydrostatic stress can lead to the formation and growth of micro-pores [29] (an alternative approach would involve the plastic deformation as driving force for ductile damage). Figure 11 shows the spatial distribution of the first principal stress as well as the hydrostatic stress for uniaxial tension. The volume-averaged strain is chosen as $\bar{\varepsilon} = 2.5\%$, which corresponds approximately to the strain level at which micro-damage occurs in the validation example (transition between segments II and III in Fig. 6). Stress peaks occur mainly in regions where narrow segments of the brittle phases are surrounded by a dominant ductile phase (see marks ① in the left part of Fig. 11). However, these characteristics of the microstructure are only a necessary but not a sufficient criterion for stress peaks, as the orientation of the narrow segments with respect to the macroscopic loading direction is also of importance. If the flux of the load is not aligned with the narrow segments of the brittle phases meaning that the brittle segment and the embedding ductile phase are locally aligned in series, no stress peaks can be observed (see marks ② in the left part of Fig. 11). Regarding the hydrostatic stress in the ductile phase, one can observe a similar behavior with the exception that highly stressed narrow segments of the ductile phase embedded in a dominant brittle phase are oriented in series with respect to the load. For the brittle as well as the ductile phases, the stress peaks can be found predominantly near the phase boundaries. At this point, it should be mentioned that for a quantitative assessment the third dimension needs to be incorporated when comparing stress peaks in the microstructure. However, the observations based on two-dimensional cross sections do give first insights in the microstructural characteristics that are predestined for damage initiation.

When looking at the same level of deformation but now considering a uniaxial compression test, one can observe approximately an inverse of the distribution of stresses in both the brittle and ductile phases compared to the tensile loading case (see Fig. 12). For the brittle phases, this means that damage will most likely occur in narrow segments that are aligned in series with an embedding dominant ductile phase with respect to the external load. The stress levels in brittle phases are similar for tension and compression. In the ductile phase, the maximal hydrostatic stress is significantly reduced in compression compared to tension. This indicates that damage will most probably occur in the brittle phases in the case of a compressive load.

The stress exceeding a critical value only at a single location in the microstructure does not necessarily indicate failure on the macroscale. Therefore, a quantile-based assessment of the relevant stress measures is more reasonable than monitoring the maximum stress value with respect to the whole microstructure. Fillafer [17] suggests the 90% quantile for the assessment of damage in steels with a dual-phase microstructure and a strong phase contrast. As the analyzed microstructure shares these characteristics, the 90% quantile is also chosen for the evaluation of the relevant stress measures (see Fig. 13).

In tension and for both phases, the stress measure assumed as most relevant for damage initiation increases for decreasing fraction of the ductile phase. The first principal stress in the brittle phases shows critically
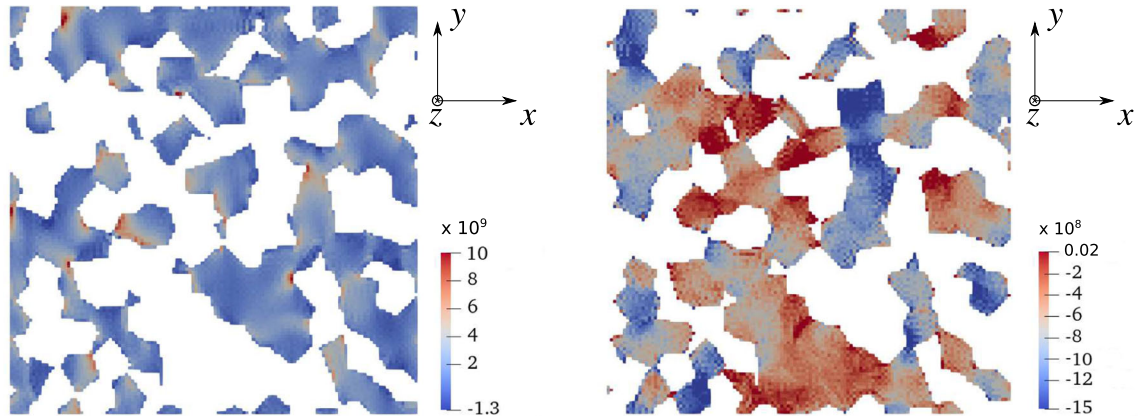
Fig. 12 Stress fields [Pa] for uniaxial compression in the x-direction at $\bar{\varepsilon} = 2.5\%$ and $P_{\text{ductile}} = 0.5$. First principal stress in the brittle phases (left) and hydrostatic stress in the ductile phase (right)
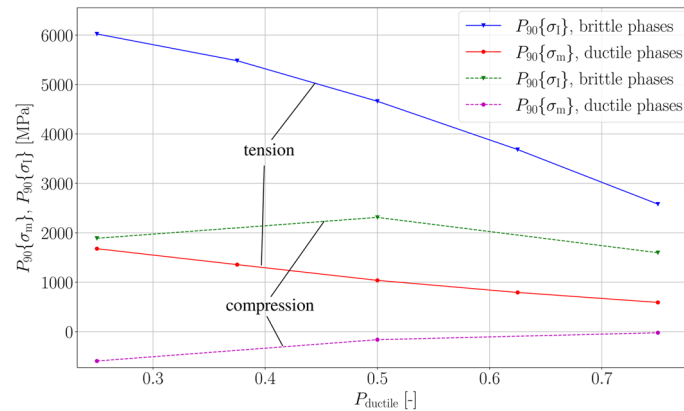

Fig. 13 90% quantiles of the relevant stresses in the brittle and ductile phases for uniaxial tension as well as compression at $\bar{\varepsilon} = \pm 2.5\%$ for varying fractions of the ductile phase

high values in the regime of the predominance of the brittle phases, which indicates a brittle failure of the microstructure. However, both stress measures approach each other in their value with an increasing fraction of the ductile phase. This indicates a possible shift from brittle to ductile damage for an increasing fraction of the ductile phase.

In compression, the level of the stress measure assumed as most relevant for damage initiation show a different trend with a varying fraction of the ductile phase. While the 90% quantile of the hydrostatic stress stays in the compressive regime for all analyzed phase fractions, the 90% quantile of the first principal stress stays on a high level hardly influenced by the fraction of the ductile phase. Still the two stress measures approach each other which makes a shift from brittle to ductile damage likely to occur for very high fractions of the ductile phase also in this load case.

5.2 Behavior of the layered composite on the macroscale

5.2.1 Thickness of the brazing layer

First, a sensitivity study on the macroscale with respect to the influence of the braze thickness on the mechanical behavior of the composite is conducted. Figure 14 shows the volume-averaged stress–strain curves (left) as well as the first principal stress averaged over 20 different paths through the layers of the composite (right). Due to similar elastic properties of the layers, the yield point of the composite is not influenced by the thickness of the brazing layer. A linear rule of mixture can be recognized from the average stress–strain curves. Except for superimposed stress peaks of second order at the interfaces between the layers the case of ideal parallel loading is recovered for $t_{\text{braze}} > 0.2\, t_{\text{comp}}$. At this point, it should be noted that the small peaks observed are artifacts
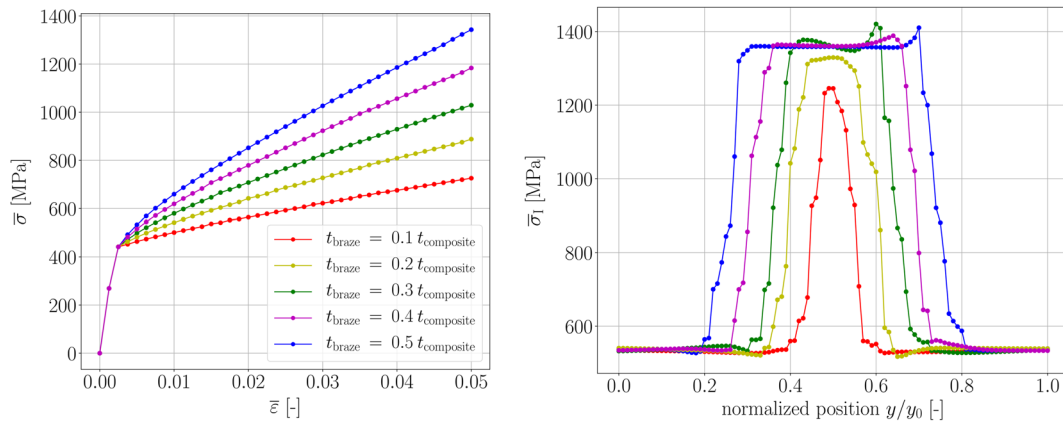
Fig. 14 Mechanical response of the layered composite for a varying braze thickness t_{braze} ($P_{ductile} = 0.5$). Left: volume-averaged stress–strain curves, right: first principal stress along paths through the layers in the y-direction at $\bar{\varepsilon} = 2.5\%$ (each data point is the mean value of 20 paths distributed in the x–z-plane)
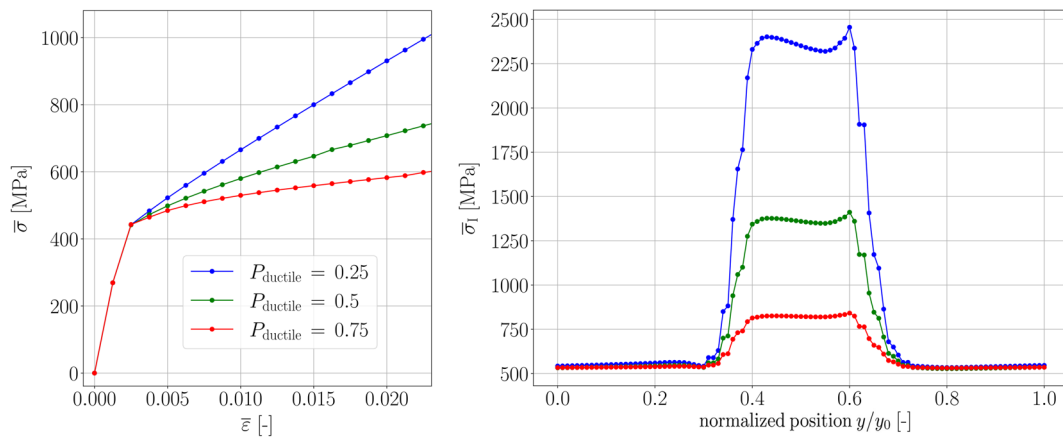

Fig. 15 Mechanical response of the layered composite for a varying fraction of the ductile phase $P_{ductile}$ ($t_{braze} = 0.3\,t_{comp}$). Left: volume-averaged stress–strain curves, right: first principal stress along paths through the layers in the y-direction at $\bar{\varepsilon} = 2.5\%$ (each data point is the mean value of 20 paths distributed in the x–z-plane)

from the modeling approach that can be reduced by further increasing the semi-periodic volume element. For braze thicknesses greater than this threshold, the stress in the brazing layer decreases continuously as the layer becomes increasingly incomplete (see Fig. 14, right). This decrease continues until no brazing layer is present, in which case the stress is homogeneously distributed.

5.2.2 Fraction of the ductile phase in the brazing layer

To assess the influence of the fraction of the ductile phase in the brazing layer on the mechanical response of the composite, the effective material behavior for three different phase fractions is transferred from the microscale to the macroscale as described in Sect. 2.2. Figure 15 shows the volume-averaged stress–strain curves (left) as well as the first principal stress averaged over 20 different paths through the layers of the composite (right). In contrast to the study of the thickness of the brazing layer, a nonlinear rule of mixture is observed. Also, the influence on the stress increase in the brazing layer is significantly higher when reducing the fraction of the ductile phase than for an increasing thickness of the brazing layer.

6 Conclusions and outlook

The comparison between the simulation results and experimental findings in the literature shows that the simulation model is capable of predicting the flow behavior of the brittle–ductile microstructure at small

plastic strains reasonably well. To reduce the mismatch between simulation and experiment for advancing deformation, the introduction of micro-damage in the brittle phases appears to be necessary. A suitable micro-damage model must incorporate local stress peaks and should be able to depict stress redistribution in the microstructure during damage evolution. The established phase field approach for damage applied to the microscale might be able to serve these demands.

The behavior of the layered composite on the macroscale approximately follows an iso-strain behavior. This makes the calibration of the micromechanical model with uniaxial tests on a layered specimen easier. Tensile tests at different temperatures and strain rates should serve as a calibration and validation basis for further model enhancements.

Furthermore, based on the simulation results the fraction of the ductile phase could be identified as a central microstructural parameter in the brazing layer, whereas variations in the morphology of the phases and in the crystallographic orientation of the grains in the ductile phase appeared as second-order effects. Compared to the thickness of the brazing layer, small fractions of the ductile phase in the brazing layer can cause a significantly higher maximum stress in the layered composite. Therefore, an increase of the fraction of the ductile phase is considered as most important for a reduction of the loads during rubbing events in turbomachinery.

Using the results from the fully numerical RVE approach, the analytical model proposed by Fischmeister and Karlsson [27] can be modified regarding the employed root function to account for the effect of stress redistribution between the ductile and the brittle phases. However, when doing so, the physical basis for such a modification has yet to be found.

Declarations

Competing interest The authors declare that they have no known competing financial interests or personal relationships that could have appeared to influence the work reported in this paper.

Appendix

A Comparison of FEM and spectral solver

As a verification of the spectral solver implemented in the DAMASK framework the σ_{xx} component of the stress field is compared for the two solution methods at a volume-averaged strain of 3%. This is done for a dual-phase microstructure with a phase fraction of the ductile phase of $P_{\text{ductile}} = 0.9$. The two methods provide a very similar solution field already for a moderate resolution of 64^3 voxels as can be seen in Fig. 16.
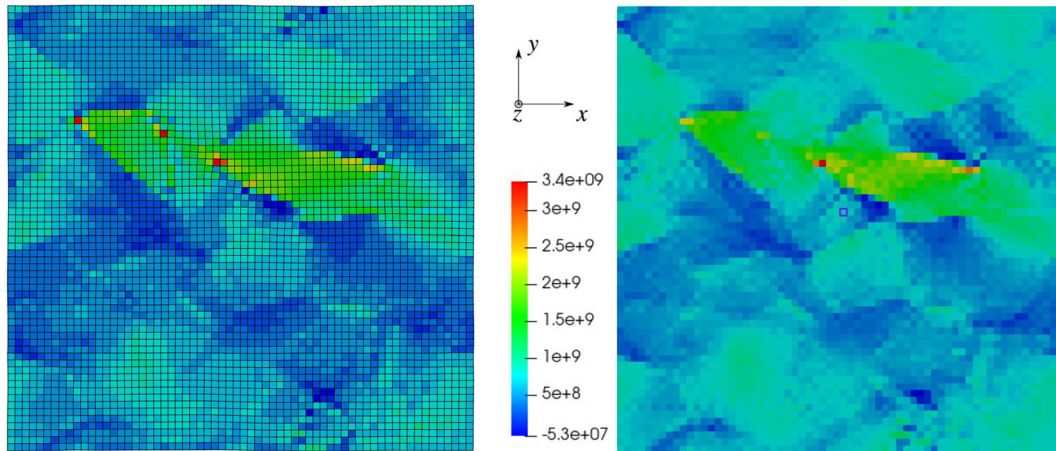
Fig. 16 Field of stress component σ_{xx} in Pa at 3% volume-averaged strain in the x-direction, FEM (left) and spectral solver (right) are presented in the same color map

B Convergence of the spectral solver

The convergence of the spectral solver with respect to the number of voxels per edge of the RVE is assessed based on the 90% quantile of the stress measures that are relevant for damage analysis. For all considered stress measures, good convergence is achieved at rather small numbers of voxels (see Fig. 17). To ensure a good approximation of the local stress fields, 128 voxels per edge of the cubic RVE are chosen.
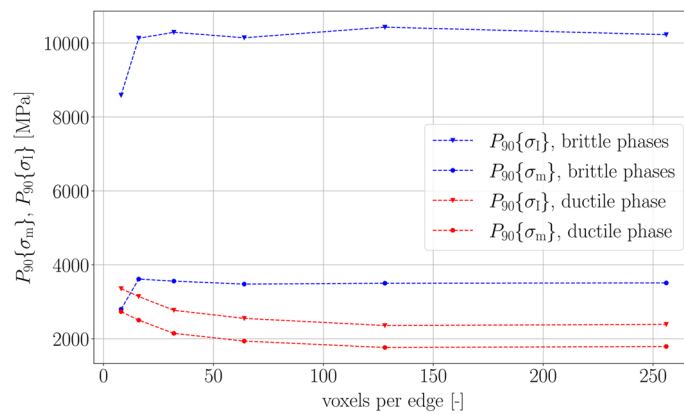

Fig. 17 Convergence of different stress measures, volume-averaged strain of $\bar{\varepsilon} = 5.0\%$

C Parameter reference configuration

Table 3 Reference configuration of geometry parameters on the microscale and the macroscale as well as reference loading conditions

	Microscale	
P_{ductile}	L_{h}	L_{RVE}
0.5	0.87 μm	10 μm
	Macroscale	
t_{comp}	t_{braze}	
200 μm	60 μm	
	Loading conditions	
$\dot{\bar{\varepsilon}}$	T	
$1\ \text{s}^{-1}$	20 °C	

D Empirical modification of semi-analytical approach

The mismatch between the results of the fully numeric RVE simulations and the semi-analytic approach by Fischmeister motivates a modification of Eq. (9). Instead of the square root the fourth root is proposed to fit the RVE simulations over the whole range of plastic strain that is considered. The modified equation reads:

$$\bar{\sigma}_{\text{ductile}} = \sigma_{\text{r,ductile}} + CG \cdot \sqrt[4]{\frac{b\bar{\varepsilon}}{\lambda_{\text{ductile}}}} \cdot \sqrt[4]{1 + \frac{P_{\text{brittle}}}{P_{\text{ductile}}} \cdot \frac{\bar{\varepsilon} - \bar{\varepsilon}_{\text{brittle}}}{\bar{\varepsilon}}}. \tag{11}$$

Figure 18 shows a significantly improved accordance between the fully numerical and the semi-analytical approaches. However, this modification is only based on an empirical analysis of the RVE simulations.
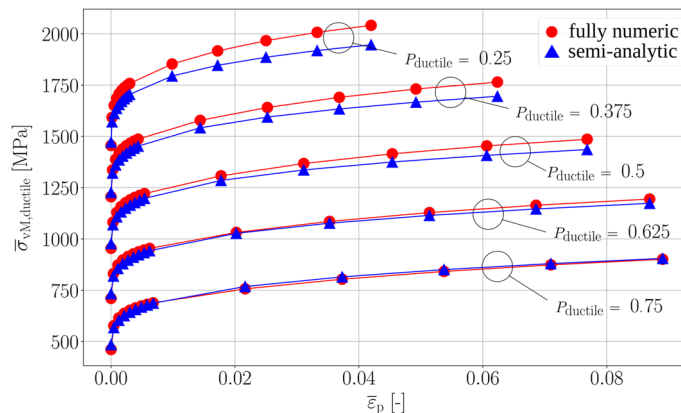

Fig. 18 Improved accordance between the fully numeric and semi-analytic approaches. Volume-averaged von Mises stress in the ductile phase containing a hard second phase plotted over plastic strain of whole aggregate. For a better readability, a successive offset of 250 MPa in the stress axis is employed for each phase fraction starting from $P_{\text{ductile}} = 0.75$

References

1. Pychynski, T., Höfler, C., Bauer, H.-J.: Experimental study on the friction contact between a labyrinth seal fin and a honeycomb stator. J. Eng. Gas Turbines Power **138**(6) (2015)
2. Abdolvand, R., Atapour, M., Shamanian, M., Allafchian, A.: The effect of bonding time on the microstructure and mechanical properties of transient liquid phase bonding between SAF 2507 and AISI 304. J. Manuf. Process. **25**, 172–180 (2017)

3. Hawk, C., Liu, S., Kottilingam, S.: Effect of processing parameters on the microstructure and mechanical properties of wide-gap braze repairs on nickel-superalloy René 108. Weld. World **61**(2), 391–404 (2017)
4. Jamaloei, A.D., Khorram, A., Jafari, A.: Characterization of microstructure and mechanical properties of dissimilar TLP bonding between IN718/IN600 with BNi-2 interlayer. J. Manuf. Process. **29**, 447–457 (2017)
5. Ulan kyzy, S., Völkl, R., Munz, O., Fischer, T., Glatzel, U.: The effect of brazing on microstructure of honeycomb liner material Hastelloy X. J. Mater. Eng. Perform. **28**(4), 1909–1913 (2019)
6. Fischer, T., Ulan kyzy, S., Munz, O., Werner, E.: Microstructure-based modelling of rubbing in polycrystalline honeycomb structures. Contin. Mech. Thermodyn. **32**(5), 1371–1383 (2019)
7. Fischer, T., Ulan kyzy, S., Munz, O., Werner, E.: Structure-property relationship of a nickel-based honeycomb sealing composite. Comput. Mater. Sci. **190**, 110270 (2021)
8. Li, Z., Schulson, E.M.: Strength, hardness and fracture toughness of a complex nickel silicide containing ductile phase particles. J. Mater. Sci. **30**(11), 2859–2865 (1995)
9. Fischer, T., Werner, E., Ulan kyzy, S., Munz, O.: Crystal plasticity modeling of polycrystalline Ni-base superalloy honeycombs under combined thermo-mechanical loading. Contin. Mech. Thermodyn. **31**(3), 703–713 (2018)
10. Ulan kyzy, S.: Werkstoffeigenschaften und Anstreifverhalten von Nickelbasis-Superlegierungen verwendet für Honig-wabenanstreifbeläge. PhD thesis, University of Bayreuth (2020)
11. Geiger, H., Scheel, K.: Handbuch der Physik, vol. 6. Springer, Berlin (1928)
12. Roters, F., Diehl, M., Shanthraj, P., Eisenlohr, P., Reuber, C., Wong, S.L., Maiti, T., Ebrahimi, A., Hochrainer, T., Fabritius, H.-O., Nikolov, S., Friák, M., Fujita, N., Grilli, N., Janssens, K.G.F., Jia, N., Kok, P.J.J., Ma, D., Meier, F., Werner, E., Stricker, M., Weygand, D., Raabe, D.: DAMASK—the düsseldorf advanced material simulation kit for modeling multi-physics crystal plasticity, thermal, and damage phenomena from the single crystal up to the component scale. Comput. Mater. Sci. **158**, 420–478 (2019)
13. Hutchinson, J.W.: Bounds and self-consistent estimates for creep of polycrystalline materials. Proc. R. Soc. Lond. A Math. Phys. Sci. **348**(1652), 101–127 (1976)
14. von Kobylinski, J., Lawitzki, R., Hofmann, M., Krempaszky, C., Werner, E.: Micromechanical behaviour of Ni-based super-alloys close to the yield point: a comparative study between neutron diffraction on different polycrystalline microstructures and crystal plasticity finite element modelling. Contin. Mech. Thermodyn. **31**(3), 691–702 (2018)
15. International Inc. Haynes. Haynes 214 alloy (UNS N07214). In: *Material Data Sheet* (2008)
16. Abaqus-Manuals. Version 6.10. *Dassault Systems Simulia Corporation* (2010)
17. Fillafer, A., Krempaszky, C., Werner, E.: On strain partitioning and micro-damage behavior of dual-phase steels. Mater. Sci. Eng. A **614**, 180–192 (2014)
18. Robl, T., Krempaszky, C., Fillafer, A., Werner, E.: Examining the unloading behavior of dual-phase steels by means of microstructure simulations. Mater. Sci. Eng. A **823**, 141744 (2021)
19. Werner, E., Wesenjak, R., Fillafer, A., Meier, F., Krempaszky, C.: Microstructure-based modelling of multiphase materials and complex structures. Contin. Mech. Thermodyn. **28**(5), 1325–1346 (2015)
20. Quey, R., Dawson, P.R., Barbe, F.: Large-scale 3d random polycrystals for the finite element method: generation, meshing and remeshing. Comput. Methods Appl. Mech. Eng. **200**(17–20), 1729–1745 (2011)
21. DeHoff, R.T., Rhines, F.N.: Quantitative Microscopy. Mcgraw-Hill, New York (1968)
22. Yadegari, S., Turteltaub, S., Suiker, A.S.J., Kok, P.J.J.: Analysis of banded microstructures in multiphase steels assisted by transformation-induced plasticity. Comput. Mater. Sci. **84**, 339–349 (2014)
23. Meier, F., Schwarz, C., Werner, E.: Crystal-plasticity based thermo-mechanical modeling of Al-components in integrated circuits. Comput. Mater. Sci. **94**, 122–131 (2014)
24. Kalpakjian, S., Schmid, S.R., Werner, E.: Werkstofftechnik, 5th edn. Pearson Studium, München (2011)
25. Kouznetsova, V.G.: Computational homogenization for the multi-scale analysis of multi-phase materials. PhD thesis, Tech-nische Universiteit Eindhoven (2002)
26. Takasugi, T., Nagashima, M., Izumi, O.: Strengthening and ductilization of Ni3Si by the addition of Ti elements. Acta Metall. Mater. **38**(5), 747–755 (1990)
27. Fischmeister, H., Karlsson, B.: Plastizitätseigenschaften grob-zweiphasiger Werkstoffe. Z. Met. **68**, 311–327 (1977)
28. Karlsson, B., Lindén, G.: Plastic deformation of ferrite-pearlite structures in steel. Mater. Sci. Eng. **17**(2), 209–219 (1975)
29. Gross, D., Seelig, T.: Bruchmechanik. Springer, Berlin (2016)